A Study of the Gamma-Ray Burst Fundamental Plane

Dainotti, M. G. [1,2,3*], Gilbertson, C. [4*], Postnikov, S. [5], Nagataki, S. [6], Willingale, R. [7]

December 9, 2024

ABSTRACT

A class of long gamma-ray bursts (GRBs) with a plateau phase in their X-ray afterglows obeys a three-dimensional (3D) relation (Dainotti et al. 2016), between the rest-frame time at the end of the plateau, T_a, its corresponding X-ray luminosity, L_a, and the peak luminosity in the prompt emission, L_{peak}, which is an extension of the two-dimensional Dainotti relation. This 3D relation identifies a GRB fundamental plane whose existence we confirmed. We extended the original analysis with X-ray data from July 2014 to July 2016 achieving a total sample of 183 *Swift* GRBs with afterglow plateaus and known redshifts. We added the most recent GRBs to the previous 'gold sample' (now including 45 GRBs) and obtained an intrinsic scatter compatible within one σ with the previous result. We compared several GRB categories, such as short with extended emission, X-ray Flashes, GRBs associated with SNe, a sample of only long-duration GRBs (132), selected from the total sample by excluding GRBs of the previous categories, and the gold sample, composed only by GRBs with light curves with good data coverage and relatively flat plateaus. We evaluated the relation planes for each of the mentioned categories and showed that they are not statistically different

[1]Department of Physics & Astronomy, Stanford University, Via Pueblo Mall 382, Stanford, CA 94305-4060, USA; mdainott@stanford.edu

[2]Obserwatorium Astronomiczne, Uniwersytet Jagielloński, ul. Orla 171, 31-501 Kraków, Poland; dainotti@oa.uj.edu.pl

[3]INAF-Istituto di Astrofisica Spaziale e Fisica cosmica, c/o CNR - Area della Ricerca di Bologna, Via Gobetti 101, I-40129 - Bologna, Italy; mariagiovannadainotti@yahoo.it

[4]Department of Physics, Virginia Tech, Blacksburg, VA 24061, USA; chrisgil@vt.edu

[5]The Center for Exploration of Energy and Matter, Indiana University, Bloomington, IN 47405, USA; postsergey@gmail.com

[6]RIKEN, Hirosawa, Wako Saitama, Japan; shigehiro.nagataki@riken.jp

[7]Department of Physics & Astronomy, University of Leicester, Road Leicester LE1 7RH, UK; zrw@le.ac.uk

[*]The first and second authors contributed equally.

from the plane derived from the gold sample and that the fundamental plane derived from the gold sample has an intrinsic scatter smaller than any plane derived from the other sample categories. We compared the jet opening angles tabulated in literature with the angles derived using the $E_{iso} - E_{gamma}$ relation of the method in Pescalli et al. (2015) and calculated the relation plane for a sample of long GRBs accounting for the different jet opening angles. We observed that this correction does not significantly reduce the scatter. In an extended analysis, we found that the fundamental plane is independent from several prompt and afterglow parameters, such as the jet opening angle, θ_{jet}, the prompt emission duration, T_{90}, the peak energy, E_{peak}, and the temporal decay index after the plateau emission, α.

Subject headings: gamma-rays bursts: general - methods: statistical

1. Introduction

Gamma-ray bursts (GRBs) have typical isotropic prompt emission energies, E_{iso}, in the range of $10^{53} erg$, and thus can be observed up to redshifts, z, of ~ 10 (Cucchiara et al. 2011). This last feature raises the tantalizing possibility of extending direct cosmological studies far beyond the redshift range covered by supernovae (SNe). However, GRBs are not yet standard candles, due to their energies spanning over several order of magnitudes. The variety of their features make it extremely difficult to categorize them under certain common patterns. Indeed, the number of sub-classes into which GRBs are grouped has grown since their discovery. GRBs are traditionally classified depending on their duration into short ($T_{90} \leq 2$ s) and long ($T_{90} \geq 2$ s) [1] (Kouveliotou et al. 1993). Later, a class of GRBs with mixed properties, such as short GRBs with extended emission (SEE), was discovered (Norris & Bonnell 2006). Long GRBs, depending on their fluence ($erg\ cm^{-2}$), can be divided into normal GRBs or X-ray Flashes (XRFs); the latter are empirically defined as GRBs with a greater fluence in the X-ray band ($2 - 30$ keV) than in the γ-ray band ($30 - 400$ keV). In addition, several GRBs also present associated SNe; hereafter they are referred as to GRB-SNe. Recently, a new category of ultra-long GRBs have been discovered (Levan et al. 2014). These GRBs present a remarkably unusual X-ray and optical lightcurves, very different from classical GRBs, with long lasting highly variable X-ray emission and optical light curves showing a small correlation with the behaviour seen in the X-ray. Levan et al. (2014) propose that these bursts, difficult to be detected, are the first examples of a new

[1] where T_{90} is the time interval over which between 5% and 95% of the total prompt energy is emitted.

population of ultra-long GRBs, that may be astrophysically relatively common. The long durations may be justified by the engine-driven explosions of stars of much larger radii than those that are usually considered for GRB progenitors, which are thought to have compact Wolf-Rayet progenitor stars. However, Levan et al. (2014) claimed that it is not possible to unequivocally identify supernova signatures within their light curves or spectra. Thus, they also consider that they may arise from the tidal disruption of stars by supermassive black holes. Other ultra-long GRBs have been observed, for example, GRB 130925A has observed features which are associated with a low metallicity blue supergiant progenitor and should characterize the class of ultra-long GRBs (Piro et al. 2014).

Regarding light curve morphology, a more complex trend in the afterglow has been observed with the *Swift* Satellite (Gehrels et al. 2004; O' Brien et al. 2006) compared to previous missions. Due to *Swift*, it has been discovered that there is a flat part, the plateau, of GRB light curves soon after the steep decay of the prompt emission. Along with these categories, several physical mechanisms for producing GRBs have also been proposed. For example, the plateau emission has mainly been ascribed to millisecond newborn spinning neutron stars, (e.g., Zhang & Mészáros 2001; Troja et al. 2007; Dall'Osso et al. 2011; Rowlinson et al. 2013,2014; Rea et al. 2015) or to accretion onto a black hole (Cannizzo & Gerhels 2009; Cannizzo et al. 2011). A very promising field has been the hunt for relations between physically meaningful GRB parameters, (e.g., Amati et al. 2002; Yonetoku et al. 2004; Ghirlanda et al. 2004; Ghisellini et al. 2008; Oates et al. 2009, 2012; Qi et al. 2009; Willingale et al. 2010), in order to employ them as cosmological indicators, as cosmological tools and as theoretical model discriminators.

The relations discovered so far suffer from having large scatters (Collazzi & Schaefer 2008), beyond observational uncertainties, highlighting that the events studied probably come from different classes of systems or perhaps from the same class of objects, but we do not yet observe a sufficiently large number of parameters to characterize the scatter. In addition, the majority of relations consider the GRB emission as isotropic, but a jet opening angle different from 90° is indeed possible. The angles are very difficult to detect due to the paucity of multi-wavelenth observations. Several methods in literature have been proposed to obtain an independent estimate of the jet opening angle (Ghirlanda et al. 2004; Goldstein et al. 2011; Lu et al. 2012; Fong et al. 2015).

As it was pointed out in Dainotti et al. (2010), in order to properly use GRB relations as reliable model discriminators and cosmological tools, it is necessary to separate the GRB categories to have a more homogeneous, observationally-motivated sample. In fact, it may be that the scatter of the relations could be higher, because we mix GRBs with different properties. Isolating GRB categories allows us to derive tighter relations, thus, increasing

the accuracy with which the cosmological parameters are inferred (e.g., Cardone et al. 2009, 2010; Dainotti et al. 2013b; Postnikov et al. 2014).

One of the first attempts to standardize GRBs in the afterglow parameters was presented by the Dainotti relation, Dainotti et al. (2008, 2010), where an approximately inversely proportional relation between the rest-frame time at the end of the plateau phase, T_a (in previous papers T_a^*), and its corresponding luminosity, L_a, was discovered. Dainotti et al. (2013a) proved through the robust statistical Efron & Petrosian (1992) method, hereafter EP, that this correlation is intrinsic, and not an artifact of selection effects or due to instrumental threshold truncation, as it is also the case for the $L_{peak} - L_a$ relation (Dainotti et al. 2011b, 2015b), where L_{peak} is the peak luminosity in the prompt emission.

In this paper we confirm results discussed in Dainotti et al. (2016), namely, that the peculiar plateau phase GRBs can be employed to isolate a sub-class of events that define a very tight plane in a three-dimensional space of $(\log L_a, \log T_a, \log L_{peak})$, see also NASA press release $http://swift.gsfc.nasa.gov/news/2016/grbs_std_candles.html$. We confirmed that the scatter of the fundamental plane is still smaller when the gold sample, a specific class of GRBs without steep plateaus and with good coverage of the data, is chosen. We have extended the previous gold sample to 45 GRBs obtaining an intrinsic scatter compatible with our previous finding within one σ. We found that other relation planes of the different categories have larger scatters than the fundamental plane derived from the gold sample. We also discovered that the fundamental plane is independent from several prompt and afterglow parameters, such as the prompt emission duration, T_{90}, the peak energy, E_{peak}, the jet opening angle, θ_{jet} and the temporal decay index after the plateau emission, α. We compared the jet opening angles tabulated in literature with the angles derived using the $E_{iso} - E_\gamma$ relation of the method in Pescalli et al. (2015), hereafter PM. Finally, we calculated the relation plane for a sample of long GRBs accounting for the different jet opening angles and we observed that it does not significantly reduce the scatter. We note that the literature angles and those derived through the PM give compatible results within 1 σ, but mainly due to the large standard deviations. They have significantly disparate plane orientations, leaving open the debate for the most reliable method to obtain these angles without having multi-wavelength observations of the afterglow. In Sections §2 and §3 we describe the *Swift* data samples used and the three-parameter relations for those sample respectively. In §4, we describe the Pescalli method. In §5, we show the relation planes using the jet opening angles to account for beam collimation. In section §6 we present the independence of the (L_a, T_a, L_{peak}) relation from other relevant prompt and afterglow parameters. In §7, we summarize our findings and conclusions.

2. Sample Selection

We analyzed 183 GRB X-ray plateau afterglows detected by *Swift* from 2005 January up to 2016 July with known redshifts, spectroscopic or photometric, available in Xiao & Schaefer (2009), on the Greiner webpage[2] and in the Gamma-ray Coordinates Network (GCN) circulars and notices[3], excluding redshifts for which there is only a lower or an upper limit. The redshift range of our sample is $(0.033, 9.4)$. We include all GRBs for which the Burst Alert Telescope (BAT) + X-Ray Telescope (XRT) light curves can be fitted by the Willingale et al. (2007), phenomenological model (hereafter W07). The W07 functional form for $f(t)$ is:

$$f(t) = \begin{cases} F_i \exp\left(\alpha_i \left(1 - \dfrac{t}{T_i}\right)\right) \exp\left(-\dfrac{t_i}{t}\right) & \text{for } \; t < T_i \\ \\ F_i \left(\dfrac{t}{T_i}\right)^{-\alpha_i} \exp\left(-\dfrac{t_i}{t}\right) & \text{for } \; t \geq T_i \end{cases} \tag{1}$$

for both the prompt (index "i=p") γ - ray and initial X-ray decay and for the afterglow ("i=a"), modeled so that the complete light curve $f_{tot}(t) = f_p(t) + f_a(t)$ contains two sets of four free parameters $(T_i, F_i, \alpha_i, t_i)$. The transition from the exponential to the power law (PL) occurs at the point $(T_i, F_i e^{-t_i/T_i})$ where the two functional forms have the same value. The parameter α_i is the temporal PL decay index and the time t_i is the initial rise timescale. We exclude the cases when the fitting procedure fails or when the determination of 1σ confidence intervals does not fulfill the Avni (1976) χ^2 prescriptions, see the XSPEC manual. Thus, we ended up with a sample of 183 GRBs[4]. We compute the source rest-frame isotropic luminosity L_a in units of erg s^{-1} in the *Swift* XRT bandpass, $(E_{min}, E_{max}) = (0.3, 10)\ keV$ as follows:

$$L_a = 4\pi D_L^2(z)\, F_X(E_{min}, E_{max}, T_a) \cdot K, \tag{2}$$

where $D_L(z)$ is the luminosity distance for the redshift z, assuming a flat ΛCDM cosmological model with $\Omega_M = 0.3$ and $H_0 = 70$ km $s^{-1} Mpc^{-1}$, F_X is the measured X-ray energy flux in (erg $cm^{-2} s^{-1}$), and K is the K-correction for cosmic expansion $(1+z)^{(\beta-1)}$, where β is

[2]http://www.mpe.mpg.de/ jcg/grbgen.html

[3]http://gcn.gsfc.nasa.gov/

[4]http://heasarc.nasa.gov/xanadu/xspec/manual/XspecSpectralFitting.html

the X-ray spectral index of the plateau phase. We downloaded the light curves from the Swift webpage repository, $http://www.swift.ac.uk/burstanalyser$, and we derived the spectral parameters following Evans et al. (2009). As shown in Dainotti et al. (2010), requiring an observationally homogeneous sample in terms of T_{90} and spectral lag properties implies removing short GRBs ($T_{90} \leq 2$ s) and SEE from the analysis. We separated the GRBs cataloged as SEE in Norris & Bonnel (2006), Levan et al. (2007), Norris et al. (2010). For the evaluation of the remaining SEE GRBs we follow the definition of Norris et al. (2010), who identify SEE events as those presenting short spikes followed, within 10 s, by a decrease in the intensity emission by a factor of 10^3 to 10^2, but with almost negligible spectral lag. Moreover, because there are long GRBs for which an associated SNe has not been detected, such as, for example the nearby $z = 0.09$ SNe-less GRB 060505, the existence of a new group of long GRBs without SNe has been suggested, thus highlighting the possibility of two types of long GRBs, with and without SNe. Therefore, in the interest of selecting an observational homogeneous class of objects, we segregate long GRBs with no associated SNe from the other categories. Under this specific criterion all the GRB-SNe that follow the Hjorth & Bloom (2011) classification are considered separately. Within the GRB-SNe sample, we applied a further classification, which is an update of the one of Hjorth & Bloom (2011). This identifies GRB-SNe sub-samples based on the quality of the identification of SNe associated to the GRB. The considered categories are: A) strong spectroscopic evidence for a SN associated with the GRB, B) a clear light curve bump as well as some spectroscopic evidence suggesting the LONG-SN association, C): a clear bump on the lightcurve consistent with the GRB-SNe association, but no spectroscopic evidence of the SN, D) a significant bump on the light curve, but the inferred SN properties are not fully consistent with other GRB-SNe associations or the bump is not well sampled or there is no spectroscopic redshift of the GRB, E) a bump, either of low significance or inconsistent with other observed GRB-SNe identifications, but with a spectroscopic redshift of the GRB. Similarly, to evaluate samples which are homogeneous regarding the ratio between γ and X-ray fluence, we separated all XRFs from the other mentioned categories. The selection criteria are applied in the observer frame.

In all that follows, L_{peak} ($erg\ s^{-1}$) is defined as the prompt emission peak flux over a 1 s interval. Following Schaefer (2007) we compute L_{peak} as follows:

$$L_{peak} = 4\pi D_L^2(z)\, F_{peak}(E_{min}, E_{max}, T_a) \cdot K, \tag{3}$$

where F_{peak} is the measured gamma-ray energy flux over a 1 s interval ($erg\ cm^{-2}s^{-1}$). To further create a sample with more homogeneous spectral features, we consider only the GRBs for which the spectrum computed at 1 s has a smaller χ^2 for a single PL fit than

for a cutoff power law (CPL). Specifically, following Sakamoto et al. (2010), when the $\chi^2_{CPL} - \chi^2_{PL} < 6$, the PL fit is preferred. We additionally discard 6 GRBs that were better fit with a blackbody model than with a PL. This full set of requirements reduces the sample to 132 long GRBs. Finally, we construct a sub-sample by including strict data quality and morphology requirements: the beginning of the plateau should have at least five data points and the plateau should not be too steep (the angle of the plateau must be less than 41°). The first of the above selection rules guarantees that the light curves clearly present the transition from the steep decay after the prompt emission to the plateau phase. The number of points required for the W07 fit should be at least four, since there are four free parameters in the model, one of which should be after the end of the plateau. Thus, the requirement of six points in total (five at the start and at least one after the plateau) ensures a minimum number of points to have both a clear transition to the plateau phase and simultaneously to constrain the plateau. This data quality cut defines the gold sample which includes 45 GRBs. We have also confirmed through the T-test that this gold sample is not statistically different from the distribution of (L_a, T_a, L_{peak}, z) of the full sample, thus showing that the choice of this sample does not introduce any biases, such as the Malmquist or Eddington ones, against high luminosity and/or high redshift GRBs. Specifically, L_a,T_a,L_{peak} and z of the gold sample present similar Gaussian distributions, but with smaller tails than the total sample (see Dainotti et al. 2015a); thus there is no shift of the distribution toward high luminosities, larger times, or high redshift. So the selection cut naturally removes the majority of the high error outliers of the variables involved, thus reducing the scatter of the relation for the gold sample.

We analyzed separately from the gold sample the following GRB categories: SEE (Norris & Bonnel 2006; Levan et al. 2007; Norris et al. 2010), the complete GRB-SNe sample (Hjorth & Bloom 2011), the sub-sample of GRBs spectroscopically associated with SNe (classifications A, B, and C from Hjorth & Bloom 2011), XRFs, and long GRBs excluded from the ultra-long GRB category and the previous categories.

3. The 3D Relation for Long GRBs, XRF, SEE, GRB-SNe, and the Gold Sample

Figure (1) shows all 183 GRBs in the (L_a, T_a, L_{peak}) parameter space, divided in five categories: GRB-SNe (cones), X-ray flashes (spheres), SEE (cuboids), long GRBs (circles), and ultra-long GRBs (polyhedrons). Darker colors indicate data points above the plane, while lighter colors indicate data points below the plane. It can be noted that the separate sub-classes of GRBs show greater spread about the plane than the long GRB sample. Using

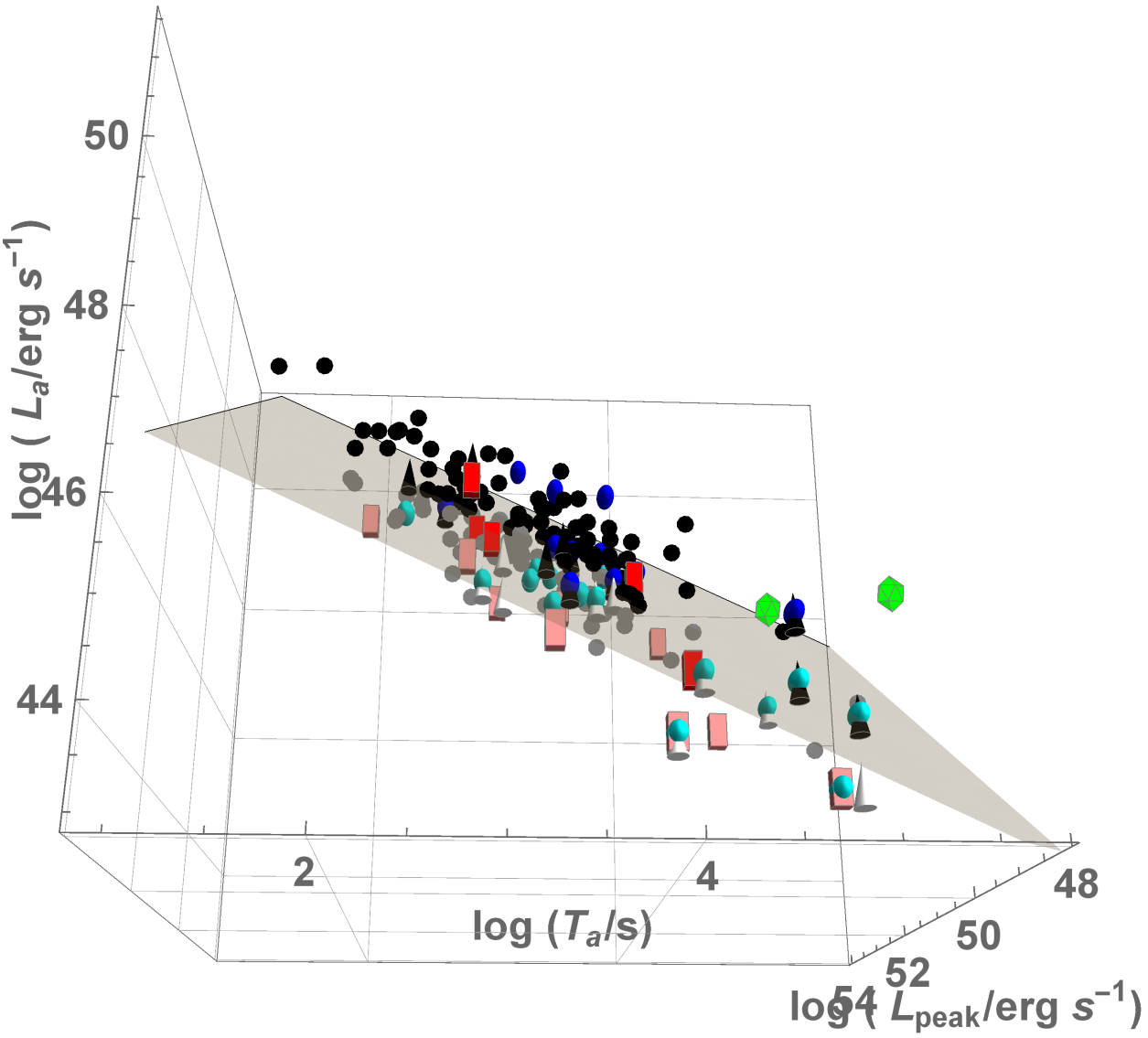

Fig. 1.— 183 GRBs in the (L_a, T_a, L_{peak}) space, with a plane fitted using the 183 GRBs, including GRB-SNe (cones), X-ray flashes (spheres), SEE (cuboids), long GRBs (circles), and ultra-long GRBs (polyhedrons). Darker colors indicate data points above the plane, while lighter colors indicate data points below the plane.

the method described in Dainotti et al. (2016), we use the parameters L_a, T_a, and L_{peak} to create a best-fit plane for the GRB categories. When we parametrize this plane using the angles θ and ϕ of its unit normal vector, the following formula is used:

$$\log L_a = C_o - \cos(\phi)\tan(\theta)\log T_a - \sin(\phi)\tan(\theta)\log L_{peak} \tag{4}$$

where $C_o = C(\theta, \phi, \sigma_{int}) + z_o$ is the normalization of the plane correlated with the other variables, θ, ϕ and σ_{int}; while z_o is the uncorrelated fitting parameter related to the normalization and C is the covariance function. For simplicity, we will rewrite the previous formula in the following way:

$$\log L_a = C_o + a \times \log T_a + b \times \log L_{peak} \tag{5}$$

where $a(\theta, \phi) = -\cos(\phi)\tan(\theta)$ and $b(\theta, \phi) = -\sin(\phi)\tan(\theta)$. This normalization of the plane allows the resulting parameter set, θ, ϕ, σ_{int} and z_o to be uncorrelated and provides explicit error propagation. For example, with the updated gold sample, we get a new optimal plane:

$$\log L_a = (17.65 \pm 5.7) - (0.83 \pm 0.10)\log T_a + (0.64 \pm 0.11)\log L_{peak}, \tag{6}$$

where $C_o = (17.65 \pm 5.7)$, $a = -(0.83 \pm 0.10)$ and $b = (0.64 \pm 0.11)$. All of the fits shown in this paper were performed using the D'Agostini method (D'Agostini 2005). Uncertainties are always given as 1σ.

For the updated gold plane $\sigma_{int} = 0.316 \pm 0.039$, which is within 1σ of the previously obtained value. The R^2_{adj} for the gold sample has slightly increased to 0.81, and remains comparable to the original gold sample. R^2_{adj} gives a version of the coefficient of determination, R^2, which is adjusted for the number of parameters in the model. The Pearson correlation coefficient, r, is 0.90 with a probability of the same sample occurring by chance, $P = 1.75 \times 10^{-17}$. The normalization of the plane, $C(\sigma_{int}, \phi, \theta)$, is given by:

$$C = 13.90 - 62.28\theta^2 - 0.29\sigma_{int} + 0.38\sigma^2_{int} - 8.23\phi - 0.05\sigma_{int}\phi + 15.13\phi^2 + \theta(99.62 - 0.10\sigma_{int} + 90.31\phi). \tag{7}$$

The correlation was also calculated for all of the mentioned GRB sub-classes. The values for these fits are shown in Table (1) which shows sub-samples in order of increasing scatter, σ_{int}. The panels of Figures (2) and (3) show the fitted plane in projection for all mentioned sub-classes. As we can see, going from the left to the right in Figure (2), the scatter decreases from the XRF to the long sample and it further decreases when we consider the planes shown in Figure (3) going from SEE to GRB-SNe ABC, and finally reaching the smallest scatter

Category	C_o	a	b	σ_{int}	N
Gold	17.65 ± 5.68	-0.83 ± 0.1	0.64 ± 0.11	0.32 ± 0.04	45
SNe ABC	20.87 ± 6.5	-1.03 ± 0.12	0.58 ± 0.13	0.33 ± 0.08	11
SEE	14.11 ± 8.16	-1.05 ± 0.14	0.71 ± 0.16	0.39 ± 0.09	15
Long	14.52 ± 3.67	-0.87 ± 0.06	0.7 ± 0.07	0.41 ± 0.03	132
SNe Total	10.19 ± 6.55	-0.78 ± 0.12	0.77 ± 0.13	0.5 ± 0.08	22
XRF	9.03 ± 7.14	-0.71 ± 0.14	0.79 ± 0.13	0.53 ± 0.08	27

Table 1: Table of best-fit values for relation plane parameters in order of increasing scatter, σ_{int}.

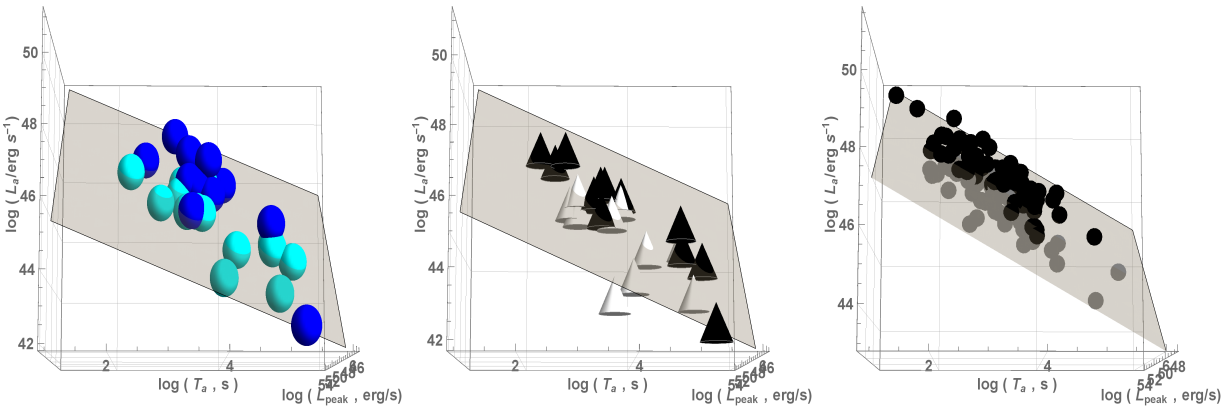

Fig. 2.— Projection of the (L_a, T_a, L_{peak}) relation, in order of decreasing intrinsic scatter, for XRF, GRB associated with SNe, and long GRB respectively.

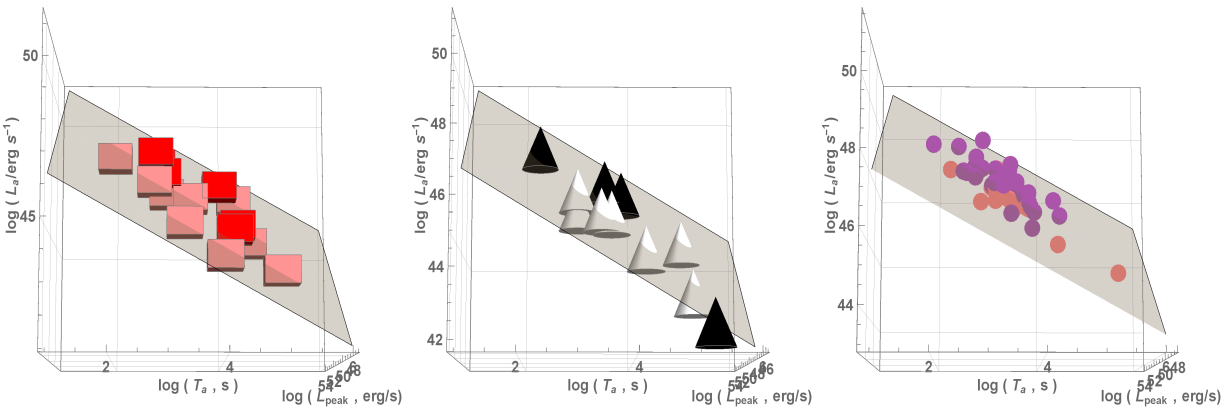

Fig. 3.— Projection of the (L_a, T_a, L_{peak}) relation, in order of decreasing intrinsic scatter, for SEE, GRBs spectroscopically associated with SNe, and the gold sample respectively.

in the right panel with the gold sample. These planes also show that the GRB-SNe ABC category, which is considerably associated with SNe, are better correlated than that of the total GRB-SNe sample. This confirms a previous study performed in a 2D parameter space using the $L_a - T_a$ correlation.

There are a few key details to notice in Table (1). Importantly, the gold sample still has the lowest intrinsic scatter of all the category fits. Another significant feature is that all of the plane parameters are within 1σ of the fundamental plane. The planes of these categories are not statistically different, thus we cannot hypothesize that these planes suggest different energy mechanisms, but we can conclude that the existence of the fundamental plane is confirmed to be driven by the gold sample features rather than the category based sampling.

It can also be shown that no category distribution is significantly separated from the fundamental plane. In Figure (4), combined plots of the distribution of GRB geometric distance from the fundamental plane are shown for each category. The center of the distributions for all of the GRB sub-categories lie within $3\sigma_{int}$ of the fundamental plane. Of note is the fact that the ultra-long GRBs can be associated with the fundamental plane. One possibility that could explain this is discussed in Greiner et al. (2015). It was found that an ultra-long GRB (GRB 111209A) was associated with a SNe, and this may indicate a magnetar origin. There are only two ultra-long GRBs in this sample, so a full analysis of this type will have to wait until a larger sample is available.

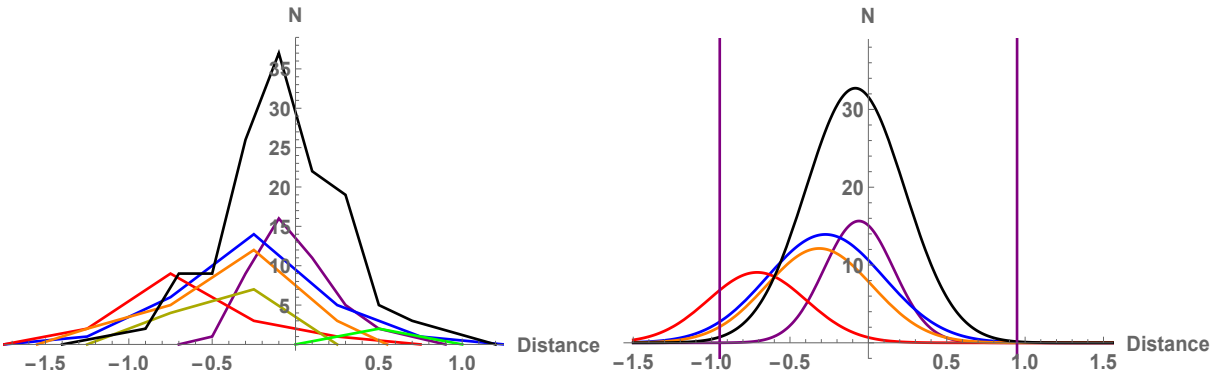

Fig. 4.— Left: A line plot showing the distance distribution from the fundamental plane for GRBs of each category, including GRB-SNe (orange), GRBs spectroscopically associated with SNe (yellow), XRF (blue), SEE (red), gold sample GRBs (purple), long GRBs (black), and ultra-long GRBs (green). Right: A plot showing Gaussian fits of the distributions displayed in the left panel, using the same color scheme. The vertical lines indicate the $3\sigma_{int}$ line from the GRB fundamental plane. Ultra-long GRBs and GRBs spectroscopically associated with SNe are not shown as they had too little data to reliably fit.

4. Deriving the Jet Opening Angle

In order to evaluate how the plane determination depends on the isotropic emission choice, we have to compute the jet opening angle. For simplicity the luminosity and energy output of GRBs are calculated assuming isotropic emission because the necessary quantity to account for the collimation of the emission, namely the jet opening angle, proves to be very difficult to acquire without simultaneous multi-wavelength observations. While several methods have been used to obtain this angle (Ghirlanda et al. 2004; Goldstein et al. 2011; Lu et al. 2012; Fong et al. 2015), we do not have this estimate for all GRBs. Thus, in order to obtain estimates for θ_{jet}, we turn to the method of Pescalli et al. (2015) in which the jet opening angle can be derived using the $E_{peak} - E_{\gamma}$ relation (Ghirlanda et al. 2004) and the $E_{peak} - E_{iso}$ (Amati et al. 2002). We use equation (8) of Pescalli et al. (2015), repeated below, to compute these angle values:

$$1 - cos\theta_{jet} = (\frac{k_A}{k_G})^{1/G} E_{iso}^{\frac{A-G}{G}} \tag{8}$$

where k_A and k_G are the normalization constants, and A and G are the slopes of the Amati and Ghirlanda relations.

From Ghirlanda et al. 2004:

$$E_{peak} = k_G \times E_{\gamma}^{G} = 267 \times (E_{iso}(1 - cos\theta_{jet})/(4.3 \times 10^{50} erg))^{0.706 \pm 0.047} \tag{9}$$

From Amati et al. 2014:

$$logE_{peak} = 0.52 \pm 0.06 \times log(E_{iso}/10^{52} erg) + 2 \tag{10}$$

or

$$E_{peak} = k_A \times E_{iso}^{A} = 100 \times (E_{iso}/10^{52} erg)^{0.52 \pm .06} \tag{11}$$

By equating and simplifying these equations, one gets the following:

$$1 - cos\theta_{jet} \approx \frac{5.36 \times 10^{11}}{E_{iso}^{0.26}} \tag{12}$$

Thus, an angle can be easily calculated for all GRBs with known E_{iso} values. In order to test the robustness and consistency of this method, we collected jet opening angles from several sources in the literature. The PM angles and angles collected from literature are shown in Table (2). For our analysis, we used only angles reported in literature which have a definite estimate and not simply upper or lower limits. For objects with multiple angle

estimates in literature, we used the average of the calculated values. The angles derived with the PM are slightly different from those found in literature. A comparison of the distribution of the jet opening angles for the same GRBs computed with the two methods and a histogram of the distribution of the total set of PM angles are shown in Figure (5). The mean values for the compared distributions are different, but not statistically. The averages of the PM angles and the literature angles for the same GRBs are 7.92±3.24° and 4.69±4.26°, respectively.

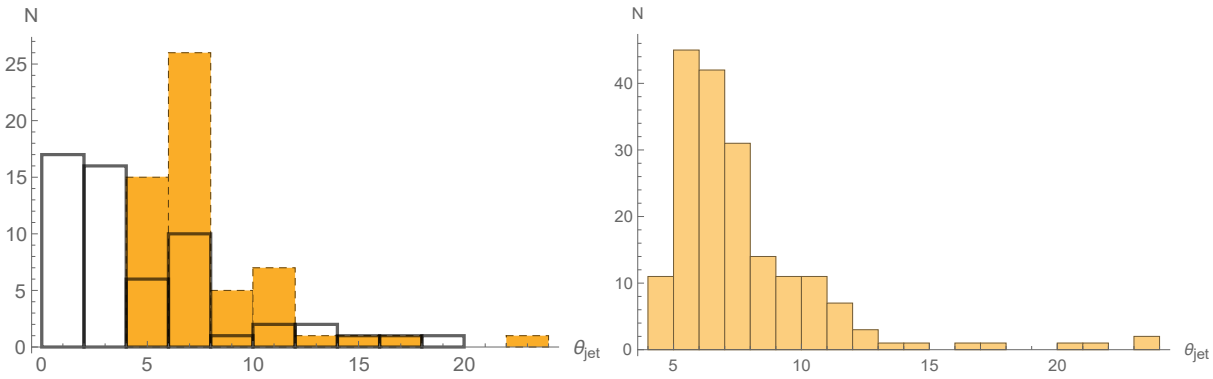

Fig. 5.— Left: A histogram showing the jet opening angle distribution for GRBs with angles available in literature. The PM angles are shown in orange. The jet opening angles found in literature are shown with the thick border. Right: A histogram showing the jet opening angle distribution for the 183 objects with the PM angles. It follows a skew normal distribution.

5. 3D Relation Planes Using the Jet Opening Angles

With the θ_{jet} derived from the PM and gathered from other literature sources, an analogous relation to the (L_a, T_a, L_{peak}) can be formed. Namely, a $(L_\gamma, T_a, L_{\gamma,peak})$ relation where:

$$L_\gamma = L_a \times (1 - cos(\theta_{jet})) \tag{13}$$

and

$$L_{\gamma,peak} = L_{peak} \times (1 - cos(\theta_{jet})) \tag{14}$$

These formulas are meant to account for the non-isotropic emission of the GRB, and they are a simple scaling factor for the luminosity, while leaving the time unchanged. Using these corrected luminosity values, and the D'Agostini plane fitting methodology as we did in §3, $(L_\gamma, T_a, L_{\gamma,peak})$ relation planes were derived for the long GRBs with the known angles. There are only 32 long GRBs which have available literature angles. This set of 32 objects will be hereafter be referred to as LLA (long literature angle set). Best-fit planes were derived

GRB ID	Z	Category	θ_{jet}, ° (PM)	θ_{jet}, ° (Literature)	References
050315	1.95	Long	6.18±0.62	∼5, 4.35±0.49	1,2
050318	1.44	Long	8.09±0.34	$3.65^{+0.25}_{-0.78}$,$4.9^{+0.3}_{-1.0}$, 2.18±0.4	2,3
050319	3.24	XRF	5.98±0.68	2.18±0.34	2
050401	2.90	Long	5.43±0.78	3.8±.65, 1.15± 0.15, ∼1	4,5,6
050505	4.27	Long	5.75±0.72	2.2-3.8, 1.66±0.26	2,7
050603	2.82	SEE	5.66±0.74	1.3-2.3	8
050730	3.97	Long	5.74±0.72	$1.6^{+0.6}_{-0.2}$	9
050802	1.71	XRF	7.41±0.36	∼ 1, 1.2±0.17	2,10
050824	0.83	XRF-E	10.86±1.39	11.46	11
050904	6.29	Long	5±0.87	8.02, $6.2^{+3.3}_{-1.4}$, 8, 1.95±0.29	2,12,13,14
060115	3.53	Long	5.91±0.68	1.89±0.34	2
060124	2.30	XRF	7.88±0.35	3.61 ±.43, 3.04±0.37	2,4
060206	4.05	XRF	6.34±0.58	2.01±0.06	2
060210	3.91	XRF	4.94±0.88	1.2±0.14	2
060218	0.03	XRF-A	23.65±9.81	17.19, 12.61±6.36	2,15
060418	1.49	Long	6.26±0.59	$22.5^{+0.9}_{-2.5}$, 1.03±0.72	2,14
060512	2.10	Long	8.07±0.41	-	-
060522	5.11	Long	5.88±0.7	-	-
060526	3.21	XRF	6.04±0.67	6.56 ±0.80, 3.61±0.06	2,4
060604	2.68	Long	7.44±0.5	∼7	16
060605	3.80	Long-Gold	6.8±0.5	$2.37^{+0.37}_{-0.10}$, 1.55±0.06	2,17
060614	0.13	XRF-SEE	11.61±1.74	11.12 ±1.4, 7.56±1.55	2,4
060707	3.43	Long	6.11±0.64	6.36±1.09	2
060714	2.71	Long-Gold	5.81±0.7	1.15±0.06	2

Table 2: Jet opening angles for the 183 objects with angles derived from the PM and collected from literature. For the rest of the table, see online material. Under Category, Long refers to long GRBs, Gold refers to gold sample GRBs, SEE refers to short GRBs with extended emission, XRF refers to an X-ray flash, Ultra refers to an ultra-long GRB (there are none in shown table), and A, B, C, D, and E indicate a GRB associated with SNe using the categories of Hjorth et al. 2011. References: 1) Vaughan et al. 2005; 2) Lu et al. 2012; 3) Perri et al. 2005; 4) Ghirlanda et al. 2007; 5) Kamble et al. 2009; 6) De Pasquale et al. 2006; 7) Hurkett et al. 2006; 8) Grupe et al. 2006; 9) Perri et al. 2007; 10) Oates, S. et al. 2007; 11) Sollerman et al. 2007; 12) Frail et al. 2006; 13) Laskar et al. 2014; 14) Cenko et al. 2010; 15) Toma et al. 2007; 16) Dai et al. 2007; 17) Ferrero et al. 2009; 18) Xu et al. 2009; 19) Grupe et al. 2010.

for the $(L_\gamma, T_a, L_{\gamma,peak})$ relation for the LLA objects corrected with the PM angles and the literature angles. Best-fit planes were also derived for the total long sample and the gold sample GRBs using the PM angles. An isotropic version of the LLA was also fitted as a comparison. The best fit values for these fits are shown in Table (3). The scatter is lower for the samples corrected with the PM angles, with the lowest scatter coming from the gold sample corrected with the PM angles. An estimate of the variance that the angle correction introduces can be found using the standard deviation of the angle distributions and gives values of ± 0.38 *log L* for the PM angles and ± 1.32 *log L* for the literature angles.

Categories	C_o	a	b	σ_{int}	N
Gold Isotropic	17.65 ± 5.68	-0.83 ± 0.10	0.64 ± 0.11	0.32 ± 0.04	45
Gold Pescalli	26.69 ± 6.81	-0.87 ± 0.10	0.44 ± 0.14	0.30 ± 0.04	45
Long Isotropic	14.52 ± 3.67	-0.87 ± 0.06	0.7 ± 0.07	0.41 ± 0.03	132
Long Pescalli	23.86 ± 4.22	-0.91 ± 0.06	0.5 ± 0.08	0.39 ± 0.03	132
LLA Isotropic	23.17 ± 7.85	-0.6 ± 0.14	0.52 ± 0.15	0.35 ± 0.05	32
LLA Pescalli	34.52 ± 9.19	-0.65 ± 0.13	0.27 ± 0.19	0.32 ± 0.05	32
LLA Literature	1.9 ± 5.45	-0.43 ± 0.14	0.91 ± 0.11	0.39 ± 0.06	32

Table 3: Table of best-fit values for relation plane parameters.

While a decrease in scatter occurs when the PM angles are used, it is well within one σ. The literature angle plane produced some interesting results. It is the only plane that is statistically different from the fundamental plane in terms of plane tilt, but we only have 32 GRBs in this sample, so a full comparison can be made only when a larger sample is available. The use of literature angles to scale the luminosity also increased the scatter. All of the other plane tilt parameters are within 1σ of the fundamental plane. The LLA planes are significantly different depending on the angles used to scale, but still have comparable scatter. Thus, we cannot conclude that the scatter of the fundamental plane is significantly reduced if we use the beamed luminosities computed with the PM angles or the angles collected from literature.

6. Independence of the Fundamental Plane from Selected Parameters

With the goal of further reducing scatter of this 3D relation, a number of independent GRB parameters were tested to see whether or not a 4D relation existed that would significantly decrease the scatter of the fundamental plane. The tested quantities included T_{90}, α, E_{peak}, and θ_{jet}.

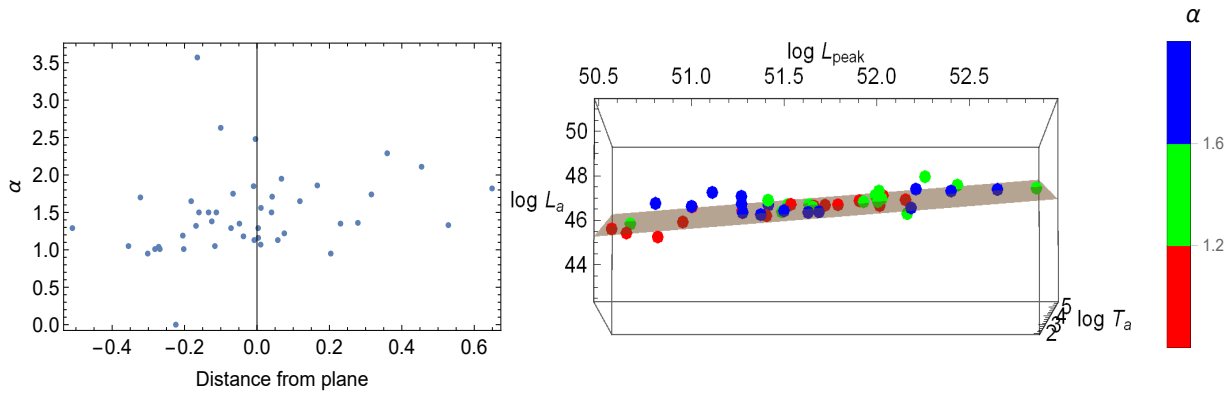

Fig. 6.— Left: A 2D plot of α over distance from the fundamental plane for the gold sample. Right: Color bar plot of fundamental plane with a color bar depending on α.

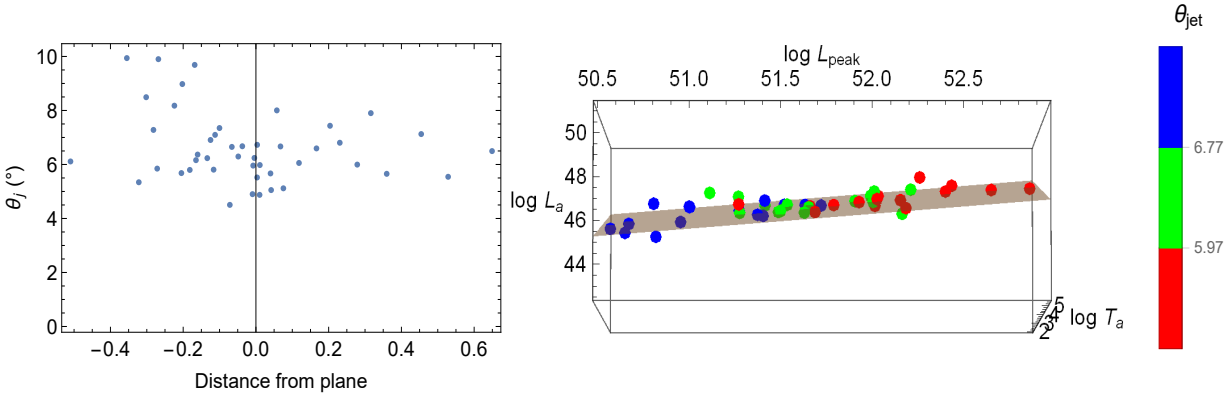

Fig. 7.— Left: A 2D plot of θ_{jet} over distance from the fundamental plane for the gold sample. Right: Color bar plot of fundamental plane with a color bar depending on θ_{jet}.

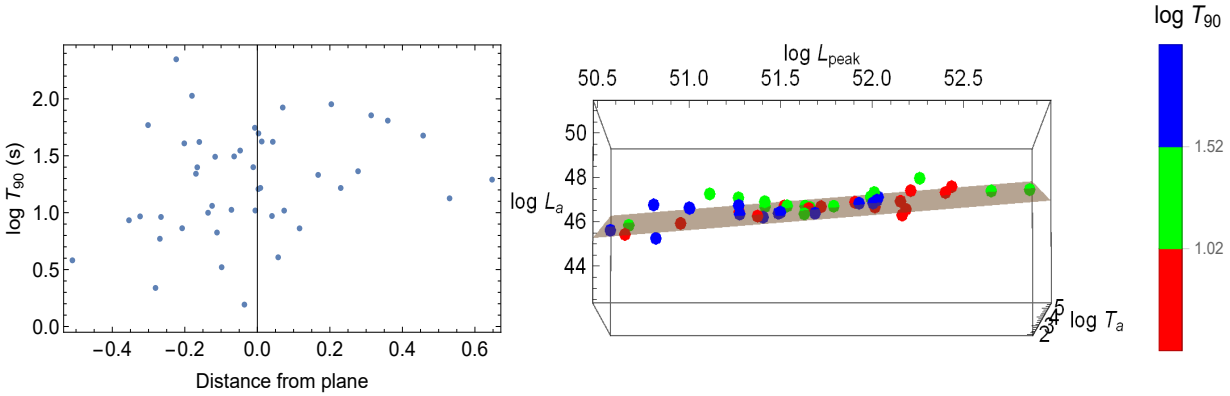

Fig. 8.— Left: A 2D plot of T_{90} over distance from the fundamental plane for the gold sample. Right: Color bar plot of fundamental plane with a color bar depending on T_{90}.

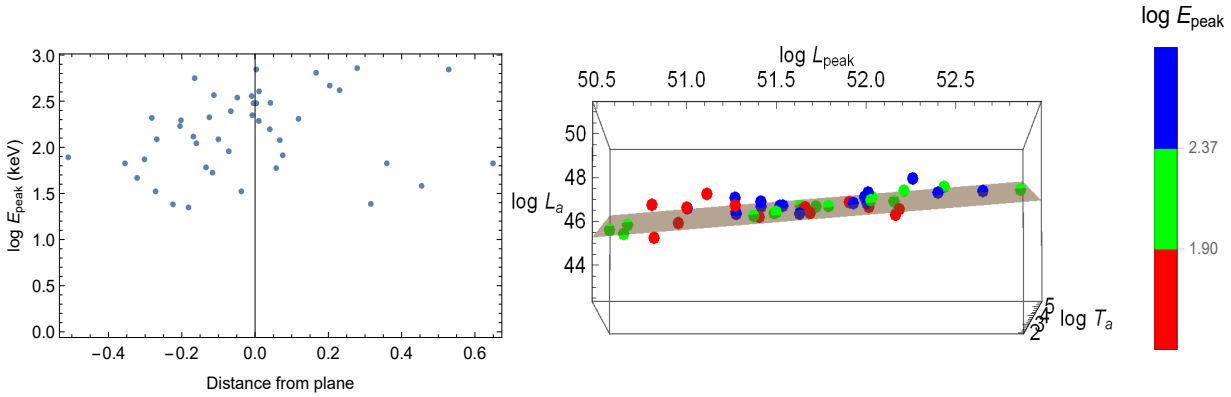

Fig. 9.— Left: A 2D plot of E_{peak} over distance from the fundamental plane for the gold sample. Right: Color bar plot of fundamental plane with a color bar depending on E_{peak}.

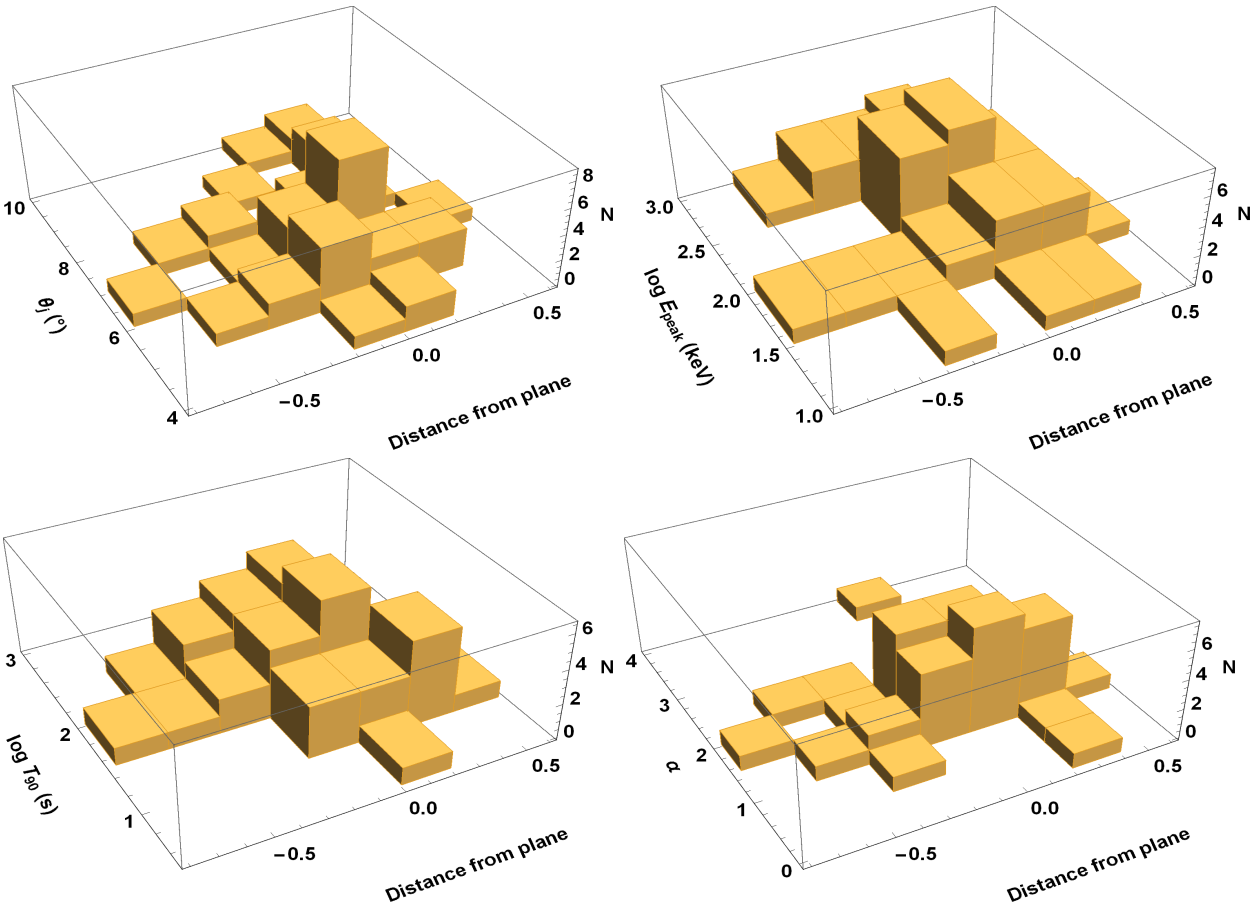

Fig. 10.— 3D histograms of the relationship between the same prompt and afterglow parameters of Figures (6)-(9) and geometric distance from the fundamental plane.

On the left panels of Figures (6)-(9), there are plots of these parameters versus the geometric distance from the fundamental plane derived with the gold sample. On the right panel of the same figures, the four-dimensional color bar plots visually show the relationship between the parameters and the positions of the points on the plane. If a correlation had existed between the parameters and the plane, a clear pattern should have been seen in the scatter and color bar plots. There are no explicit trends in the scatter plots or groupings of colors shown. The Spearman coefficient for these distributions is uniformly ≤ 0.40, confirming the lack of real correlation for these parameters[5]. The Spearman and Pearson correlation coefficients for each of the parameters versus the geometric distance from the fundamental plane is given in Table (4).

Parameter	Spearman ρ	R^2_{adj}	R	Probability
α	0.40	0.05	0.26	0.04
θ_{jet}	0.21	0.03	0.23	0.06
$logT_{90}$	0.26	0.02	0.22	0.08
$logE_{peak}$	0.30	0.02	0.20	0.09

Table 4: Statistical and correlation parameters for linear fits of the parameters versus geometric distance from the fundamental plane.

In order to inspect further visually these relations, we plot 3D histograms of the parameters and distance from the plane in Figure (10). These plots strengthen the conclusion that there is no underlying relationship between the studied variables. This outcome reinforces the previous result that the fundamental plane is independent from relevant prompt and afterglow emission parameters.

7. Conclusions

In our investigation of GRB sub-classes, we confirmed the results of Dainotti et al. (2016). Plateau phase GRBs can be used to isolate a sub-class of events that define a very tight plane in a three-dimensional space of $(\log L_a, \log T_a, \log L_{peak})$. We confirmed that the scatter of the 3D relation plane is still the smallest when the gold sample, a specific class of GRBs without steep plateaus and with good coverage of the data, is used for the fitting. The previous gold sample was extended to contain pertinent events up to July 2016, for a

[5]The Spearman coefficient is a nonparametric measure of rank correlation. A Spearman coefficient less than 0.50 generally means that the correlation is not meaningful.

total of 45 events, and an updated fundamental plane was found with an intrinsic scatter compatible within one σ of the previous finding. All other tested relation planes related to the different categories have a larger intrinsic scatter than the fundamental plane derived from the gold sample. In order to gain insight on the robustness of the fundamental plane, we explored how it can depend on a fourth parameter. We found that it is independent from several relevant prompt and afterglow parameters, namely α, T_{90}, E_{peak} and θ_{jet}. We calculated the relation planes for the LLA sample and observed that the angle corrections did not significantly decrease the plane scatter when compared to the isotropic plane. We also conclude from the comparison of the angles gathered in literature and those derived through the PM that the quest for the most reliable method to obtain these angles without having multi-wavelength observations of the afterglow is still open.

8. Acknowledgments

This work made use of data supplied by the UK Swift Science Data Centre at the University of Leicester. We are particularly grateful to M. Ostrowski for his remarkable comments and suggestions which helped improving the manuscript. M.G.D acknowledges the Marie Curie Program, because the research leading to these results has received funding from the European Union Seventh Framework Program (FP7-2007/2013) under grant agreement N 626267. C.G. acknowledges the US DOE and the SULI Program for funding his Summer research experience at SLAC. S.N. acknowledges the funding support of the JSPS.

REFERENCES

Amati L., Frontera F., Tavani M. et al. 2002, A&A, 390, 81

Amati, L. et al. 2009, A&A, 508, 173.

Amati, L. et al. 2014, ANNALEN DER PHYSIK, 526, 340.

Avni, Y. 1976, ApJ, 210, 642

Bernardini, M.G. et al. 2012, A&A, 539, 3.

Blustin, A. J., Band, D., Barthelmy, S., et al. 2006, ApJ, 637, 901

Burrows, D. N., Grupe, D., Capalbi, M., et al. 2006, ApJ, 653, 468

Cardone, V.F. et al. 2009, MNRAS, 400, 775.

Cardone, V.F., et al. 2010, MNRAS, 408, 1181.

Cannizzo, J. K. & Gehrels, N., 2009, ApJ, 700, 1047.

Cannizzo, J. K., et al. 2011, ApJ, 734, 35.

Cenko, S. B., Kasliwal, M., Harrison, F. A., et al. 2006, ApJ, 652, 490

Cenko, S. B., et al. 2010, ApJ, 711, 641

Chandra, P., et al. 2010, ApJ, 712, L31

Collazzi, A. C., & Schaefer, B. E. 2008 ApJ, 688, 456.

Cucchiara, N. et al. 2011, ApJ, 736, 7.

Curran, P. A., van der Horst, A. J., Beardmore, A. P., et al. 2007, A&A, 467, 1049

D' Agostini, G. 2005, arXiv : physics/0511182

Dall'Osso, S. et al. 2011, A&A, 526A, 121D

Dai, X. et al. 2007, ApJ, 658, 509

Dainotti, M. G. et al. 2008, MNRAS 391L, 79.

Dainotti, M.G. et al. 2010, ApJL, 722, L215.

Dainotti, M. G. et al. 2011a, ApJ, 730, 135.

Dainotti, M.G. et al. 2011b, MNRAS, 418, 2202.

Dainotti, M.G., et al. 2013, ApJ, 774, 157.

Dainotti, M.G., et al. 2013b, MNRAS, 436, 82.

Dainotti, M.G., et al. 2015a, ApJ, 800, 31.

Dainotti, M.G., et al. 2015b, MNRAS, 451, 4.

De Pasquale, M., Beardmore, A. P., Barthelmy, S. D., et al. 2006, MNRAS, 365, 1031

Efron, B. & Petrosian, V., 1992, ApJ, 399, 345.

Enderli, M., et al. 2016, ArXiv e-prints

Evans, P. A., et al. 2009, MNRAS, 397, 1177

Ferrero, P., Klose, S., Kann, D. A., et al. 2009, A&A, 497, 729

Fong, W., et al. 2014, ApJ, 780, 118

Fong, W., et al. 2015, ApJ, 815, 102F.

Frail D.A. et al. 2006, ApJ, 646, L99

Gerhels, N. et al. 2004, ApJ, 611, 1005.

Ghirlanda, G., et al. 2004, ApJ, 616, 331.

Ghirlanda G., Nava L., Ghisellini G., Firmani C., 2007, A&A, 466, 127

Ghisellini, G., et al. 2008, A&A, 496, 3, 2009.

Goldstein, A., et al. 2011, ArXiv e-prints

Greiner, J., Mazzali, P. A., Kann, D. A., et al. 2015, Nature, 523, 189

Grupe, D., Brown, P. J., Cummings, J., et al. 2006, ApJ, 645, 464

Grupe, D., et al. 2007, ApJ, 662, 443

Grupe, D., et al. 2010, ApJ, 711, 1008

Guidorzi, C., Mundell, C. G., Harrison, R., et al. 2014, MNRAS, 438, 752

Hjorth, J., & Bloom, J.S, 2011, 'Gamma-Ray Bursts", eds. C. Kouveliotou, R. A. M. J. Wijers, S. E. Woosley, Cambridge University Press, 2011.

Hurkett, C. P. et al. 2006, MNRAS, 368, 1101

Izzo, et al. 2015, A&A, 582A, 115.

Jia, L. W. et al. 2012, RAA, 12, 411

Kamble, A., Misra, K., Bhattacharya, D., et al. 2009, MNRAS, 394, 214

Kouveliotou, C., et al. 1993, ApJ, 413, L101.

Kumar, P. & Panaitescu, A., 2008, MNRAS, 391, L19

Laskar, T., Berger, E., Tanvir, N., et al. 2014, ApJ, 781, 1

Laskar, T., Berger, E., Margutti, R., et al. 2015, ApJ, 814, 1

Levan, A. J., et al. 2007, MNRAS, 378, 1439

Lloyd, N., & Petrosian, V. ApJ, 1999, 511, 550.

Lu, R., et al. 2012, ApJ, 745, 168.

Marshall, F. E., Antonelli, L. A., Burrows, D. N., et al. 2011, ApJ, 727, 132

Mundell, C. G., et al. 2007, ApJ, 660, 489

Nakauchi D., Kashiyama K., Suwa Y., Nakamura T., 2013, ApJ, 778, 67

Nappo, F., Pescalli, A., Oganesyan, G., et al. 2016, arXiv:1604.08204

Nicuesa Guelbenzu, A., Klose, S., Rossi, A., et al. 2011, A&A, 531, L6

Nicuesa Guelbenzu, A., Klose, S., Greiner, J., et al. 2012, A&A, 548, A101

Norris, J.P & Bonnell, J.T. 2006, ApJ, 643, 266.

Norris, J.P., Gehrels, N. & Scargle, J. 2010, ApJ, 717, 411.

O' Brien, P.T., Willingale, R., Osborne, J. et al. 2006, ApJ, 647, 1213.

Oates, S. R., de Pasquale, M., Page, M. J. et al. 2007, MNRAS, 380, 270

Oates, S. R. et al. 2012, MNRAS, 426L,86.

Perri, M., et al. 2005, A&A, 442, L1

Perri, M., Guetta, D., Antonelli, L. A., et al. 2007, A&A, 471, 83

Piro, L. et al. 2014, ApJ, 790L, 15.

Pescalli, A., et al. 2015, MNRAS, 447, 1911

Postnikov, S., et al. 2014, ApJ, 783, 126.

Qi, S., Lu, T., & Wang, F.-Y., 2009, MNRAS, 398, L78

Rea, N . et al. 2015, ApJ 813, 92.

Rossi, A., Schulze, S., Klose, S., et al. 2011, A&A, 529, A142

Rowlinson, A. et al. 2013, MNRAS, 430, 1061.

Rowlinson, A. et al. 2014, MNRAS, 443, 1779.

Sakamoto, T. et al. 2011, ApJS, 195, 2.

Schaefer, B. 2007, ApJ, 660, 16.

Shao, L. & Dai, Z. G. 2007, ApJ, 660, 1319.

Soderberg, A. M., et al. 2006, ApJ, 650, 261

Soderberg, A. M., et al. 2007, ApJ, 661, 982

Sollerman, J., Fynbo, J. P. U., Gorosabel, J., et al. 2007, A&A, 466, 839

Starling, R. L. C., Rol, E., van der Horst, A. J., et al. 2009, MNRAS, 400, 90

Stratta, G. et al. 2007, A&A, 474, 827

Toma, K., Ioka, K., Sakamoto, T., & Nakamura, T. 2007, ApJ, 659, 1420

Troja, E. et al. 2007, ApJ, 665, 599

Troja, E. et al. 2016a, ApJ, 827, 102T

Troja E., et al., 2016b, preprint

Tsutsui, R., et al. 2009, JCAP, 08, 015.

Vaughan, S., et al. 2005, ApJ 638, 920

Wang, Y et al. 2016, 818,167

Willingale, R. W. et al., ApJ, 2007, 662, 1093.

Willingale, R. et al. 2010, MNRAS, 403, 1296.

Wózniak, P. R., Vestrand, W. T., Panaitescu, A. D., Wren, J. A., Davis, H. R., and White, R. R. 2009, ApJ, 691, 495

Xiao, L. & Schaefer, B.E. 2009, ApJ, 707, 387.

Xu, M., Huang, Y.-F. & Lu, T., 2009, RAA, 9, 1317

M. Xu & Y. F. Huang, A&A 2012, 538, 134.

Yonetoku, D. et al. 2004, ApJ, 609, 935.

Zhang, B & Mészáros, P. 2001, ApJ, 552L, 35.

This preprint was prepared with the AAS LaTeX macros v5.2.